ACS APPLIED MATERIALS & INTERFACES

www.acsami.org

Research Article

Cellular and Molecular Insights into the Divergence of Neural Stem Cells on Matrigel and Poly-L-lysine Interfaces

Cuiping Wu,[‖] Suru Liu,[‖] Lei Zhou,[‖] Zhengnong Chen, Quanjun Yang, Yaqi Cui, Ming Chen, Linpeng Li, Bingbing Ke, Chunyan Li,[*] and Shankai Yin[*]

Cite This: *ACS Appl. Mater. Interfaces* 2024, 16, 31922−31935

Read Online

ACCESS | Metrics & More | Article Recommendations | Supporting Information

ABSTRACT: Poly-L-lysine (PLL) and Matrigel, both classical coating materials for culture substrates in neural stem cell (NSC) research, present distinct interfaces whose effect on NSC behavior at cellular and molecular levels remains ambiguous. Our investigation reveals intriguing disparities: although both PLL and Matrigel interfaces are hydrophilic and feature amine functional groups, Matrigel stands out with lower stiffness and higher roughness. Based on this diversity, Matrigel surpasses PLL, driving NSC adhesion, migration, and proliferation. Intriguingly, PLL promotes NSC differentiation into astrocytes, whereas Matrigel favors neural differentiation and the physiological maturation of neurons. At the molecular level, Matrigel showcases a wider upregulation of genes linked to NSC behavior. Specifically, it enhances ECM−receptor interaction, activates the YAP transcription factor, and heightens glycerophospholipid metabolism, steering NSC proliferation and neural differentiation. Conversely, PLL upregulates genes associated with glial cell differentiation and amino acid metabolism and elevates various amino acid levels, potentially linked to its support for astrocyte differentiation. These distinct transcriptional and metabolic activities jointly shape the divergent NSC behavior on these substrates. This study significantly advances our understanding of substrate regulation on NSC behavior, offering novel insights into optimizing and targeting the application of these surface coating materials in NSC research.

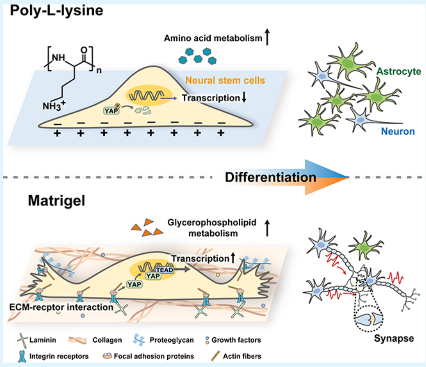

KEYWORDS: *Neural stem cell, Matrigel, Poly-L-lysine, Differentiation, Electrophysiological function, YAP, Metabolomics*

1. INTRODUCTION

Neural stem cells (NSCs) are a group of uncommitted progenitor cells, which are capable of self-renewal and generating neurons, astrocytes, and oligodendrocytes or their committed progenitors.[1] Expanding NSCs and guiding their differentiation toward the preferred lineage are promising approaches for regenerative medicine, drug discovery, and pathogenesis research for nervous system disorders.[2,3] Generally, NSCs do not tend to adhere easily to untreated substrates, so surface modification is essential for NSC culture. Optimizing the interface of biomaterials to achieve better applications for NSCs and neural regeneration is a continually advancing area of innovation. This encompasses breakthroughs in surface topology,[4] electroactive biomaterials,[5] composite nerve scaffolds,[6,7] bioprinting applications,[8] and more. However, the complex preparation processes associated with these advanced interfaces often hinder their widespread adoption in conventional laboratory settings. Commercial coatings, primarily comprising non-extracellular matrix (ECM) components represented by poly-L-lysine (PLL)[9−12] and ECM components represented by Matrigel,[13−15] are still the most widely used for substrate modification. These interfaces not only provide a conducive microenvironment for NSC growth but also play a crucial role in determining the molecular signaling and fate of NSCs.[16] Therefore, they also serve as essential components in composite materials for interface optimization.[17,18] However, the specific effects of these interfaces on the molecular and cellular behavior of NSCs are not well understood. This knowledge gap hinders the informed coating selection for various research objectives and could potentially affect result consistency across studies using different substrates.

The biochemical and biophysical cues of the interface are two major factors that regulate NSC behavior.[19] Matrigel, an ECM extract from murine Englebreth-Holm-Swarm tumors, is enriched with laminin, collagen IV, heparan sulfate proteoglycans, entactin, and growth factors like basic fibroblast growth factor (bFGF), and transforming growth factor-beta.[20] ECM proteins can interact with receptors on NSCs (such as the laminin-integrin interaction), and the growth factors can trigger specific molecular signaling pathways. These composite

Received: February 14, 2024
Revised: May 22, 2024
Accepted: May 23, 2024
Published: June 14, 2024

https://doi.org/10.1021/acsami.4c02575

components better mimic the *in vivo* cell microenvironment than individual ECM proteins, orchestrating vital cellular processes such as adhesion, migration, self-renewal, and differentiation.[21] On the contrary, PLL, a polyamino acid comprised of lysine sequences, is positively charged for a broad pH range. It promotes cell adhesion in a nonreceptor mediated and nonspecific manner via an electrostatic bond with negatively charged cell membranes.[22] Besides biochemical cues, NSCs perceive various mechanical signals like substrate stiffness and topography, converting them into intracellular biochemical messages through mechanotransduction. Crucial mechanotransduction pathways, such as Hippo/YAP (Yes-associated protein) signaling, regulate transcription to direct cellular behaviors, including cytoskeletal rearrangement, migration, proliferation, and differentiation.[23] Furthermore, growing evidence indicates a connection between stem cell metabolic activity and diverse biochemical and biophysical signals originating from the cellular microenvironment.[24,25] NSCs experience substantial metabolic alterations during differentiation, such as the shift from glycolysis to oxidative phosphorylation.[26] Additionally, there have been reports of crosstalk between glucose metabolism and ECM mechanical properties, such as stiffness.[27] These information inspired us to investigate the distinct effects of PLL and Matrigel, characterized by diverse biochemical and biophysical properties, on NSC behavior and underlying mechanisms by analyzing the transcriptome and metabolome profiles.

Here, we discovered that Matrigel displays superior physical properties, enhancing NSC adhesion and proliferation, and guiding NSC differentiation toward functional neurons. Conversely, PLL tends to promote NSC differentiation into astrocytes. Furthermore, through comprehensive transcriptomic and metabolomic analyses, we unveiled the intricate molecular mechanisms underlying the divergent NSC behavior on these substrates. Matrigel activates the transcriptional regulator YAP and favors glycerophospholipid metabolism, whereas PLL prefers various amino acid metabolic pathways. Overall, this study adds significantly to our understanding of how these classical interfaces distinctly regulate the cellular and molecular behavior of NSCs.

2. EXPERIMENTAL SECTION

2.1. Ethical Statement. All animal care and experimental procedures were approved by the Institutional Animal Care and Use Committee of Shanghai Sixth People's Hospital affiliated to Shanghai Jiao Tong University School of Medicine (NO. DWLL2023−0533).

2.2. Preparation and Characterization of PLL and Matrigel Substrates. Coating solution was prepared by diluting PLL (0.1 mg/mL, Sangon) and Matrigel (1:200, approximately 0.05 mg/mL, Corning) with cold phosphate buffered saline (PBS). Tissue culture-treated polystyrene plates or glass coverslips, commonly used for cell cultures, served as controls. The plates or coverslips were immersed in 1 mL/well coating solution for 6-well plates and 300 μL/well for 24-well plates, then incubated for 2 h at 37 °C. PLL substrate underwent two PBS washes for 5 min each before drying for use. Matrigel substrate was used immediately after aspiration of the coating solution. Surface chemical composition of the substrates was analyzed using a Thermo Scientific K-alpha spectrometer for X-ray photoelectron spectroscopy (XPS) measurements. Morphology and modulus were examined via Atomic force microscopy (AFM) using a Bruker Dimension Icon microscope, with the DMT modulus employed to determine Young's modulus. Surface hydrophilicity was assessed by measuring water and cell culture medium contact angles using the sessile-drop method on an optical contact angle measuring device (Biolin Theta Flex, Sweden).

2.3. Isolation and Culture of Primary Mouse NSCs. Primary NSCs were isolated from the cortex of E13.5 fetal C57BL/6 mice as previously reported.[28] The cells were cultured in a proliferation medium comprising Dulbecco's modified Eagle's medium (DMEM, Gibco) supplemented with 2% B27 (Gibco), 1% N-2 (Gibco), 20 ng/mL epidermal growth factor (PeproTech), and 20 ng/mL bFGF (PeproTech). Culturing was performed at 5% CO_2 and 37 °C. Neurospheres were dissociated into single cells using Accutase (Sigma) for passaging and subsequent experiments. For differentiation experiments, cells were plated on substrates for 24 h and then the proliferation medium was replaced with differentiation medium, comprising DMEM/Nutrient Mixture F-12 medium (Gibco) supplemented with 2% B27, 1% fetal bovine serum (Gibco), and 1 μM retinoic acid (Sigma).

2.4. Scanning Electron Microscopy (SEM). Cells were fixed with 2.5% glutaraldehyde at 4 °C overnight and postfixed with 1% osmic acid solution at 4 °C for 1 h. Then, samples were dehydrated with 30%, 50%, 70%, 80%, and 90% ethanol gradients for 15 min each, and then dehydrated with 100% ethanol 3 times for 20 min each. After critical point drying treatment for 1.5 h, the samples were sputter-coated with gold film. SEM images were obtained by field emission scanning electron microscopy (SU8010, Hitachi, Japan).

2.5. Immunofluorescence Staining. Cells were fixed with 4% paraformaldehyde for 15 min, permeabilized with 0.5% Triton X-100 for 15 min, and blocked with 5% goat serum for 30 min at 37 °C. Following this, primary antibodies were applied and left overnight at 4 °C, including rabbit anti-vinculin (1:100, Abcam), mouse anti-nestin (1:200, Abcam), rabbit anti-Ki67 (1:500, Abcam), rabbit anti- Class III beta-tubulin (Tuj1, 1:500, Abcam), mouse anti-glial fibrillary acidic protein (GFAP, 1:300, Cell Signaling Technology), mouse anti-Olig2 (1:300, Sigma), rabbit anti-myelin basic protein (MBP, 1:100, Cell Signaling Technology), mouse anti-tau (1:500, Novus), and rabbit anti-synaptophysin (1:500, Abcam). Subsequently, secondary antibodies were applied for 1 h at room temperature, including goat anti-mouse IgG H&L Alexa Fluor 488 (1:500, Abcam), goat anti-rabbit IgG H&L Alexa Fluor 555 (1:500, Invitrogen), and phalloidin-iFluor 488 (binding to F-actin, 1:1000, Abcam). Finally, Fluoroshield with 4′,6-diamidino-2-phenylindole (DAPI, Sigma) was used to label nuclei and preserve fluorescence. Images were obtained by confocal laser scanning microscopy (LSM 710, ZEISS, Germany).

2.6. Cell Proliferation Assay. 5-ethynyl-2′-deoxyuridine (EdU) assay was performed using the Cell Proliferation Kit with Alexa Fluor 488 (Beyotime) following the manufacturer's guidelines. EdU, an analog of thymidine, is incorporated into newly synthesized DNA. EdU was added to the cell culture medium at a final concentration of 10 μM and incubated for 2 h. Following fixation with 4% paraformaldehyde for 15 min and permeabilization with 0.5% Triton X-100 for 15 min, cells were exposed to click reaction solution for 30 min at room temperature in the dark. DAPI (Sigma) was used to label the nuclei. Images were obtained by confocal laser scanning microscopy (LSM 710, ZEISS, Germany). EdU-positive and DAPI-positive cells were counted using the ImageJ software (NIH, Bethesda, MD).

The cell counting kit-8 (CCK-8) assay was performed using the CCK-8 Cell Counting Kit (Vazyme). A total of 1×10^4 cells/well were plated in 96-well plates. After 0, 1, 2, 3, and 4 days of proliferation, CCK-8 solution was added and incubated at 37 °C for 3 h. The optical density (OD) value was measured at 450 nm using a microplate reader (iMark, Bio-Rad, USA). Experiments were performed in five replicates.

2.7. Morphological Analysis. Morphological analysis of NSC-derived neurons was performed using ImageJ software as previously reported.[28] Based on the immunofluorescence images of Tuj1-positive neurons after 7 days of differentiation, the neurites of the neurons were traced by the Simple Neurite Tracer plugin, and the morphological properties were quantitatively analyzed. The dendritic complexity index (DCI) was calculated as the following formula (number of branch tips + number of branch orders)/number of

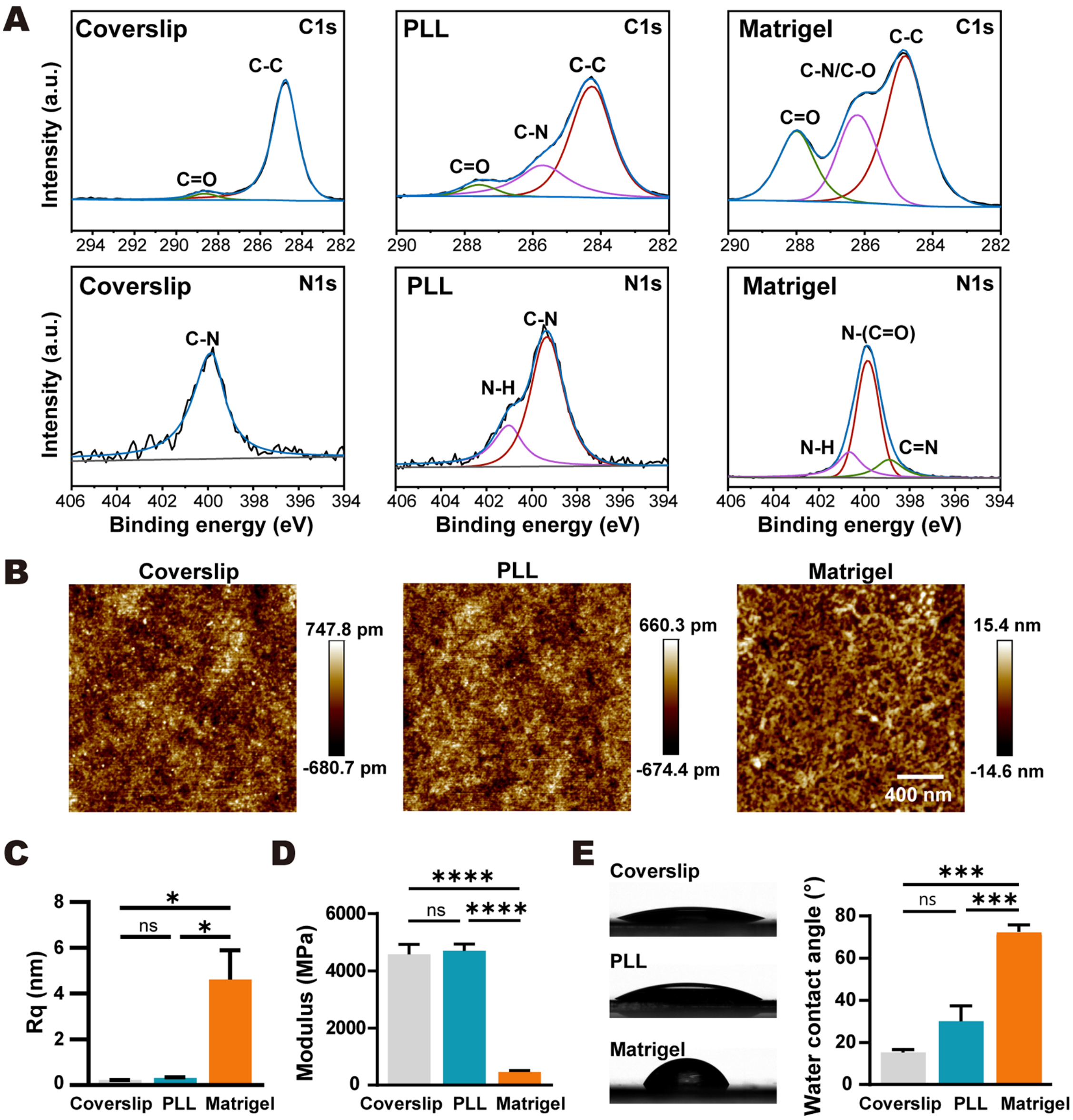

Figure 1. Characterization of biophysical and biochemical properties of PLL and Matrigel substrates. (A) High resolution of XPS C 1s and N 1s spectra of uncoated, PLL, and Matrigel-coated substrates. (B) AFM images of different substrate surfaces. (C) Rq of different substrate surfaces. $n = 3$. (D) Modulus of different substrates. $n = 3$. (E) Water contact angles of different substrate surfaces. $n = 3$. One-way ANOVA with Tukey's multiple correction test. The data are presented as the mean ± s.e.m. $^{*}P < 0.05$, $^{***}P < 0.001$, $^{****}P < 0.0001$, ns, not significant.

primary dendrites × total arbor length.[29] The Sholl Analysis plugin was used to analyze the neurite complexity of the NSCs-derived neurons at a step distance of 3 μm.

2.8. Western Blot. After 2 days of proliferation, cells were lysed in RIPA buffer containing protease inhibitors and phosphorylase inhibitors (Beyotime). Cell lysates were centrifuged and the supernatants were collected. Protein concentration was quantified using BCA Protein Assay Kit (Epizyme), mixed with sample loading buffer, and boiled for 10 min. Equal amounts of protein samples were separated by 10% SDS-PAGE and transferred to nitrocellulose membranes. The membranes were blocked with 5% BSA for 1 h at room temperature and then incubated with primary antibodies overnight at 4 °C, including rabbit anti-YAP (1:1000, Cell Signaling Technology), rabbit anti-phospho-YAP (1:1000, Cell Signaling Technology), and rabbit anti-GAPDH (1:1000, Abclonal). Subsequently, the membranes were incubated with HRP-conjugated secondary antibodies (1:1000, Abclonal) for 2 h at room temperature. Finally, signals were examined using an enhanced chemiluminescence substrate (Vazyme) and images were acquired with a chemiluminescence imaging system (Clinx Science Instruments Co., Ltd., China).

2.9. Electrophysiological Recordings. Whole-cell patch-clamp recordings were performed after 7 and 14 days of differentiation. Cells were immersed in extracellular solution consisting of (in mM): 150 NaCl, 5 KCl, 1 $MgCl_2$, 2 $CaCl_2$, 10 HEPES, and 10 glucose, pH 7.4. Recording pipettes (tip resistance 3−6 MΩ) were filled with intracellular solution contained (in mM): 140 K-gluconate, 2 $MgCl_2$, 1 $CaCl_2$, 11EGTA, 10 HEPES, and 4 Mg-ATP, pH 7.4. Whole-cell currents and membrane potentials were recorded using an EPC-10 patch-clamp amplifier (HEKA). Data were acquired at 10−20 kHz and filtered at 1−3 kHz using a computer equipped with the Pulse 6.0 software (HEKA, Lambrecht). Cells were recorded at a holding potential of −60 mV unless specifically mentioned. To examine whether action potentials (APs) could be induced, voltage responses were evoked using 500 ms steps ranging from −25 to +25 pA in 5 pA intervals. The properties of APs were analyzed based on the first AP evoked in response to a depolarizing step. Data analysis was performed using Clampfit 10.5 (Axon Instruments) and MiniAnalysis software (Synaptosoft, Fort Lee, NJ, USA).

2.10. RNA-seq and Analysis. After 7 days of differentiation, total RNA was extracted using the TRIzol reagent (Invitrogen). RNA purity and quantification were evaluated using the NanoDrop 2000 spectrophotometer (Thermo Scientific, USA). RNA integrity was assessed using the Agilent 2100 Bioanalyzer (Agilent Technologies, Santa Clara, CA, USA). Libraries were constructed using VAHTS Universal V6 RNA-seq Library Prep Kit according to manufacturer's instructions. The transcriptome sequencing and analysis were conducted by OE Biotech Co., Ltd. (Shanghai, China). The libraries were sequenced on an llumina Novaseq 6000 platform and 150 bp paired-end reads were generated. Raw reads of fastq format were first processed using fastp1 and the low quality reads were removed to obtain the clean reads. The clean reads were mapped to the reference genome using HISAT22. FPKM of each gene was calculated and the read counts of each gene were obtained by HTSeq-count4. Principal component analysis was performed using R (v 3.2.0) to evaluate the biological duplication of samples. Differential expression analysis was performed using the DESeq25. q value <0.05 and foldchange >2 or foldchange <0.5 were used as the threshold for significant differential expression genes (DEGs). Gene Ontology (GO) enrichment and Kyoto encyclopedia of genes and genomes (KEGG) pathway analysis of the DEGs were performed through Metascape online database (http://metascape.org). Gene Set Enrichment Analysis (GSEA) was performed using GSEA software. The plugin iRegulon of Cytoscape software is used to predict transcription factors. The results are visualized using an online platform (https://www.bioinformatics.com.cn) and R (v 3.2.0).

2.11. GC-MS and LC-MS Metabolomic Analysis. Integrated untargeted metabolomic analysis using Gas Chromatography−Mass Spectrometry (GC-MS) and Liquid Chromatography Mass Spectrometry (LC-MS) was performed. For each group, 6 samples were prepared for metabolite extraction. After 7 days of differentiation, cells were washed twice with cold PBS, collected with a cold mixture of methanol/water (4:1, v/v), and immediately frozen in liquid nitrogen. Extraction, metabolite identification, and quantification were performed by Shanghai OE Biotech. Co., Ltd. (Shanghai, China). Briefly, the samples were analyzed on an Agilent 8890−5977B gas chromatography system and Waters ACQUITY UPLC I-Class plus/Thermo QE spectrometer. The original LC-MS data were processed by software Progenesis QI V2.3 (Nonlinear, Dynamics, Newcastle, UK) and the GC-MS raw data were transferred to. abf format via software Analysis Base File Converter and then were imported into software MS-DIAL for further analysis. The obtained matrix was imported in R to carry out Orthogonal Partial Least-Squares-Discriminant Analysis (OPLS-DA) to distinguish the metabolites that differ between groups. To prevent overfitting, 7-fold cross-validation and 200 Response Permutation Testing were used to evaluate the quality of the model. Variable Importance of Projection (VIP) values obtained from the OPLS-DA model were used to rank the overall contribution of each variable to group discrimination. A two-tailed Student's t test was further used to verify whether the metabolites of difference between groups were significant. Differentially expressed metabolites (DEMs) were selected with VIP values greater than 1.0 and P values less than 0.05. Metabolic pathway enrichment analysis of the identified DEMs was performed based on the KEGG database.

2.12. Data Analysis. Western blot and fluorescence images were analyzed using ImageJ software and its plug-ins. Data were statistically analyzed and plotted using GraphPad Prism 9.3.1 (San Diego, California). All data are presented as the means ± standard error of the mean (s.e.m.). Group comparisons were performed using unpaired two-tailed *t tests* for two groups. One-way or two-way analysis of variance (ANOVA) was used for data comparison among multiple experimental groups. To determine statistical significance, P values <0.05 were considered statistically significant.

3. RESULTS AND DISCUSSION

3.1. Biophysical and Biochemical Characterization of PLL and Matrigel Substrates. Given the significance of biophysical and biochemical properties in cell behavior regulation, we investigated the chemical composition, surface morphology, stiffness, and wettability of glass coverslip coated with or without PLL and Matrigel. First, XPS was used to assess surface chemistry changes postcoating. Figure S1A shows the wide scan spectra of the substrates and atomic ratios of C, N, and O. PLL and Matrigel-coated substrates exhibited increased N ratios (0.95% to 3.94% and 11.66%, respectively) compared to the control, confirming successful coating. The high resolution C 1s spectra displayed new peaks at 285.7 eV (C−N) and 286.19 eV (C−N/C-O) for PLL and Matrigel-coated substrates, respectively, compared to the control (Figure 1A). N 1s spectra showed two peaks at 399.31 eV (C−N) and 401 eV (N−H) for the PLL substrate and three peaks at 398.89 eV (C═N), 399.83 eV (N−(C═O)), and 400.65 eV (N−H) for the Matrigel substrate. These functional groups can be attributed to the abundant amine and amide groups that were widely present in peptides or proteins. The introduction of surface amine functional groups might facilitate cell adhesion by providing a positively charged surface that attracts negatively charged biomolecules like proteins or cells, as previous studies demonstrated.[30]

AFM was then used to estimate substrate roughness and modulus (Figure 1B-D). The PLL substrate exhibited a smooth surface with a root-mean-square roughness (Rq) of 0.32 ± 0.03 nm, comparable to the control (0.22 ± 0.01 nm, $n = 3$, $P = 0.9953$). However, the Matrigel coating significantly increased surface roughness with an Rq of 4.62 ± 1.27 nm ($n = 3$, $P = 0.0129$). As previously reported, the Matrigel coating formed an associative network rather than a monolayer of proteins on the substrate, which may contribute to the elevation of substrate roughness.[31] In addition, PLL coating had no significant effect on coverslip modulus (uncoated vs PLL: 4586 ± 338.2 MPa vs 4703 ± 234.7 MPa, $n = 4$, $P = 0.9370$). In contrast, Matrigel coating markedly reduced substrate modulus to 457.7 ± 55.25 MPa ($n = 4$, $P < 0.0001$), providing a softer surface. The elevated surface roughness and decreased modulus have been reported to favor NSC proliferation and neural differentiation.[32,33]

The surface wettability of these substrates was evaluated by contact angle measurements. All of these substrates exhibited hydrophilic properties, with contact angles below 90°for water or cell culture medium (Figure 1E and Figure S1B). The water contact angles of uncoated, PLL, and Matrigel-coated substrates were 15.21 ± 1.34°, 30.20 ± 7.12°, and 72.58 ± 3.27°, respectively. While surface wettability's impact on cell adhesion varies due to factors like surface roughness, chemical groups, and cell types, cells typically exhibit better adhesion on surfaces with moderate wettability (water contact angles 40−70°) compared to surfaces that are highly hydrophilic or hydrophobic.[34,35] Therefore, the Matrigel substrate's moderate hydrophilicity may promote superior cell adhesion compared to the uncoated and PLL substrate. Taken together, these findings imply that while both PLL and Matrigel can provide hydrophilic adhesive interfaces for NSC growth, their diverse biochemical and biophysical characteristics may influence NSC behavior differently.

3.2. Growth Behavior of NSCs on PLL and Matrigel. Cell growth on substrates undergoes a sequential series of steps. Cells first attach to the substrate, then flatten and spread their bodies. Subsequent organization of the actin skeleton and focal adhesion formation strengthens adhesion, ultimately triggering cellular behaviors such as survival, migration, and

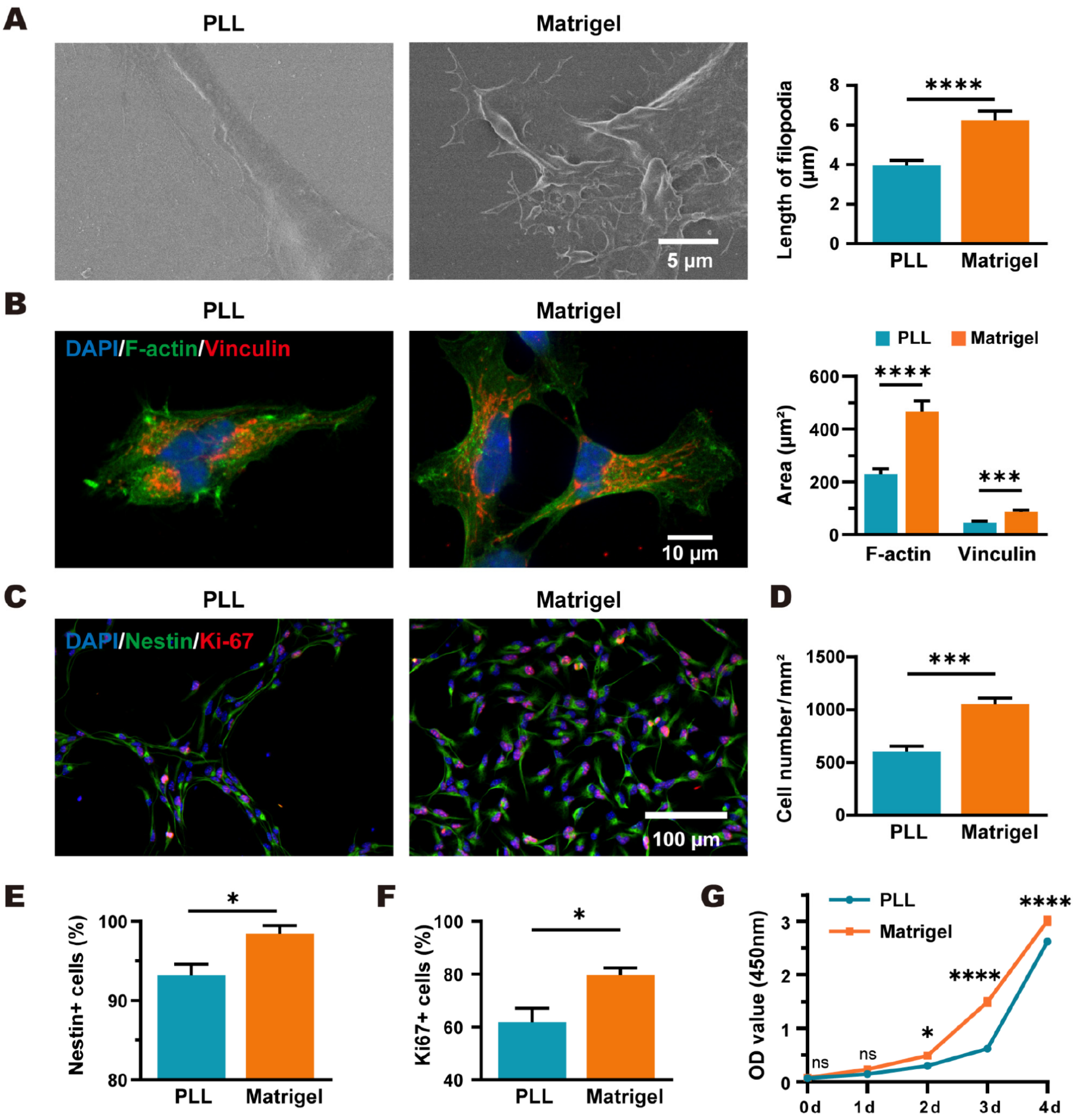

Figure 2. Adhesion, spreading, and proliferation of NSCs on Matrigel and PLL. (A) SEM images of NSCs. Bar graph shows the length of filopodia. More than 20 cells were measured. (B) Fluorescence images of NSCs with phalloidin (F-actin, green), vinculin (red), and cell nuclei (blue) after 2 days of proliferation. Bar graphs show the quantification of cell spreading area and focal adhesion area. $n = 12$ cells. (C−F) Fluorescence images of NSCs showing cell nuclei (blue), NSC marker nestin (green), and proliferation marker Ki-67 (red) after 2 days of proliferation. Bar graphs show cell number and percentage of nestin+ and Ki-67+ cells. $n = 3$. (G) Cell growth was assessed by CCK-8 assay, measured daily. $n = 5$. Two-tailed unpaired Student's t test (A−F) or two-way ANOVA with Šidák's multiple comparisons test (G). The data are presented as the mean ± s.e.m. $^{*}P < 0.05$, $^{***}P < 0.001$, $^{****}P < 0.0001$, ns, not significant.

proliferation.[36] To observe these behaviors, single NSCs were plated on substrates coated with or without PLL and Matrigel. As expected, NSCs did not adhere as a monolayer on uncoated plates or coverslips, forming floating neurospheres instead (Figure S2A). After 6 h, most NSCs on PLL remained round, while those on Matrigel displayed notable flattening and many extending processes (Figure S2B). After 2 days, NSCs on PLL clustered tightly, while those on Matrigel were evenly dispersed. SEM revealed longer filopodia in NSCs on Matrigel (6.25 ± 3.62 μm) compared to PLL (3.95 ± 2.15 μm, $P < 0.0001$) (Figure 2A and Figure S2C). Phalloidin staining and vinculin immunostaining were performed to visualize cell spreading and focal adhesions (Figure 2B). Vinculin is a crucial focal adhesion protein that links the actin cytoskeleton to adhesion receptor complexes, regulating cell adhesion and migration. NSCs on Matrigel displayed a well-organized cytoskeleton, exhibiting approximately twice the spreading area (466.0 ± 40.55 μm^2) compared to NSCs on PLL (228.0 ± 22.02 μm^2, $P < 0.0001$). Furthermore, focal adhesion areas were significantly larger on Matrigel (85.61 ± 7.74 μm^2) than on PLL (45.49 ± 5.56 μm^2, $P = 0.0004$). These results highlight Matrigel as a conducive substrate for NSC spreading and stable adhesion formation compared to PLL.

We then compared cell viability and migration on these substrates which relies on adhesion and are critical for neural tissue engineering. Live−dead cell staining showed a high percentage of live cells on both PLL and Matrigel under both proliferation (PLL vs Matrigel: 89.34 ± 0.87% vs 94.91 ±

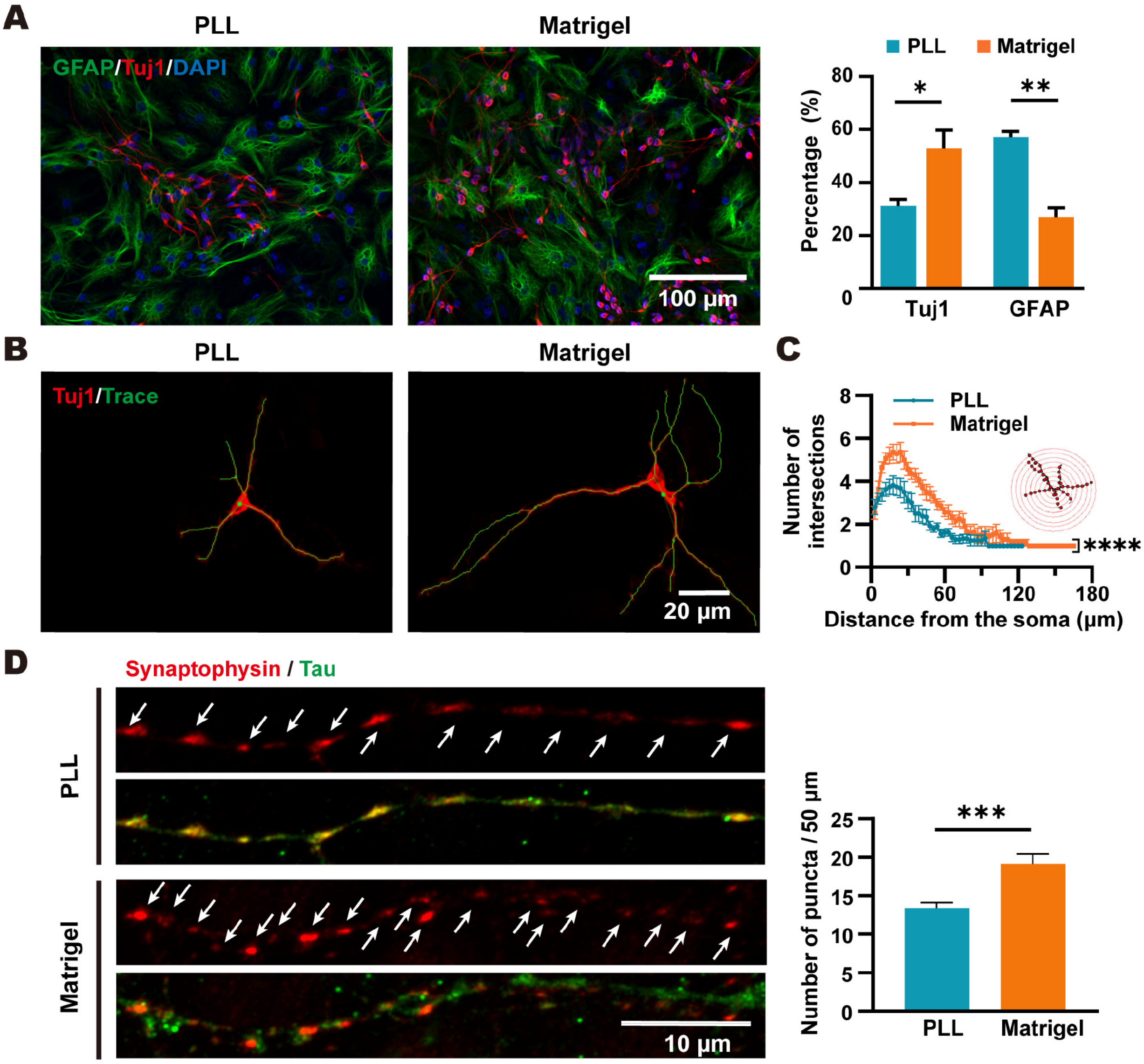

Figure 3. NSC differentiation and synaptic connection of NSC-derived neurons on PLL and Matrigel. (A) Representative fluorescence images of NSCs cultured on Matrigel and PLL after 7 days of differentiation with the neuron marker Tuj1 (red) and astrocyte marker GFAP (green). Nuclei stained with DAPI (blue). Bar graphs show the quantification of the percentage of Tuj1+ and GFAP+ cells. $n = 3$. (B) Representative neuron morphology reconstruction (green) based on Tuj1 (red) fluorescence images. (C) Sholl analysis of NSC-derived neurons. The number of neurites that intersect concentric circles at varying distances from the soma was counted (PLL, $n = 16$ neurons; Matrigel, $n = 14$ neurons). (D) Representative fluorescence images of the presynaptic marker synaptophysin (red) and the axonal marker Tau (green) after 14 days of differentiation. Bar graph shows number of synaptophysin puncta (indicated by white arrows) per 50 μm. $n = 16$ neurons. Two-tailed unpaired Student's t test (A and D), two-way ANOVA test (C). All data are presented as mean ± s.e.m. $^{*}P < 0.05$, $^{**}P < 0.01$, $^{***}P < 0.001$, $^{****}P < 0.0001$, ns, not significant.

0.43%, $n = 3$, $P < 0.0001$) and differentiation conditions (PLL vs Matrigel: 93.11 ± 0.52% vs 95.47 ± 0.46%, $n = 3$, $P = 0.0037$) (Figure S3A), suggesting that these substrates are nontoxic to NSC cultures. As expected, NSCs on Matrigel exhibited greater migration from the neurospheres, approximately 3.30 times farther than on PLL by day 2 (PLL vs Matrigel: 509.51 ± 81.83 μm vs 1681.21 ± 143.08 μm, $n = 4$, $P = 0.0004$) (Figure S3B).

Proliferation is a critical characteristic of NSCs and underlies their *in vitro* expansion. To evaluate NSC proliferation on different substrates, we conducted nuclear staining and immunostaining for nestin (NSC marker) and Ki-67 (proliferation marker) after 2 days of proliferation (Figure 2C−F). As expected, most cells on both substrates were nestin-positive, slightly higher on the Matrigel (PLL vs Matrigel: 93.16 ± 1.42% vs 98.43 ± 1.04%, $n = 3$, $P = 0.0402$), suggesting that both substrates support the maintenance of NSC stemness. There were 1.74 times more cells on Matrigel (1051 ± 59.95/mm^2) compared to PLL (604 ± 51.21/mm^2, $n = 3$, $P = 0.0002$). Ki-67 positive cells were also higher on Matrigel (79.62 ± 2.76%) compared to PLL (61.83 ± 5.24%, $n = 3$, $P = 0.0398$). In addition, the EdU incorporation assay, visualizing DNA replication during proliferation, showed a higher EdU incorporation rate on Matrigel (PLL vs Matrigel: 54.34 ± 1.93% vs 61.95 ± 1.87%, $n = 3$, $P = 0.0120$) (Figure S3C). The CCK-8 assay also confirmed significantly higher cell proliferation rates for NSCs on Matrigel at 2, 3, and 4 days of proliferation ($n = 5$, $P = 0.0170$, <0.0001, and <0.0001,

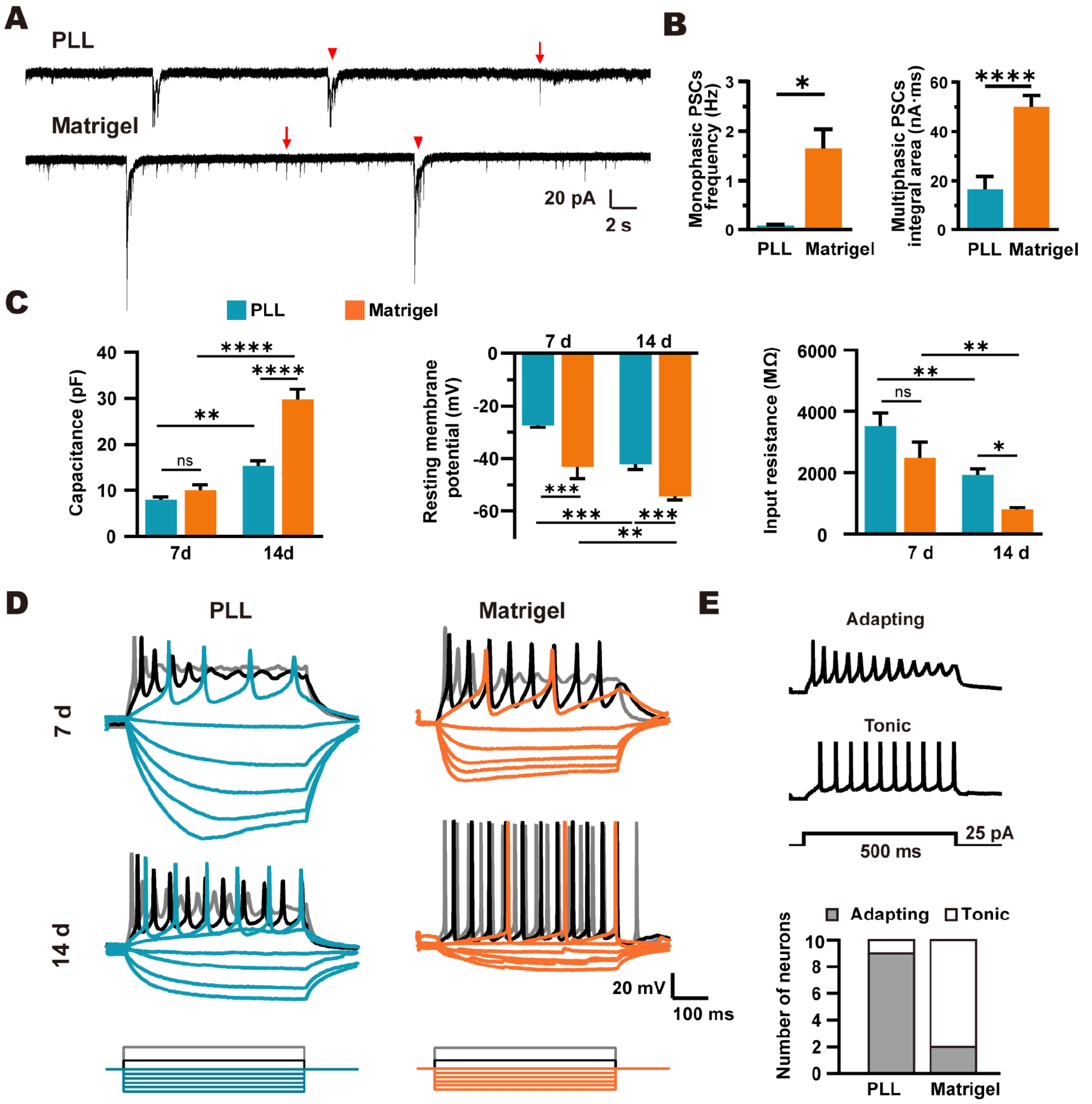

Figure 4. Physiological maturation of NSC-derived neurons on PLL and Matrigel. (A) Representative traces of spontaneous PSCs of NSC-derived neurons after 14 days of differentiation. Arrows indicate monophasic PSCs, and arrowheads indicate multiphasic PSCs. (B) Frequency of monophasic PSCs and integral area of multiphasic PSCs. Ten neurons were analyzed in each group. (C) Capacitance, RMP, and input resistance of NSCs-derived neurons after 7 and 14 days of differentiation. 7−12 cells were analyzed in each group. (D) Membrane voltage responses to hyperpolarizing (−25 pA to 0 pA in 5 pA increments) and depolarizing (10 and 25 pA) current steps. Cells were clamped at −60 mV membrane potential. (E) Representative traces of two firing patterns: adapting or tonic. Bar graph shows the number of neurons exhibiting adapting or tonic firing patterns after 14 days of differentiation. Two-tailed unpaired Student's *t* test (B) or two-way ANOVA test with Tukey's multiple comparisons test (C). Data are presented as mean ± s.e.m. $^*P < 0.05$, $^{**}P < 0.01$, $^{***}P < 0.001$, $^{****}P < 0.0001$, ns, not significant.

respectively) (Figure 2G). Overall, both PLL and Matrigel support NSC proliferation, yet Matrigel provides a more conducive environment, fostering a highly proliferative state of NSCs compared to PLL.

3.3. NSC Differentiation and Synaptic Connection of NSC-Derived Neurons on PLL and Matrigel.

NSCs possess the capacity to differentiate into neurons, astrocytes, and oligodendrocytes. Neurons, responsible for transmitting nerve impulses, are crucial in neural regeneration therapy. Astrocytes, pivotal in regulating the neural environment and supporting neuronal functions, have been associated with various neurological and psychiatric disorders when dysfunctional. Therefore, investigating NSC differentiation into distinct cell types holds significance for neural development, injury repair, and disease treatment. To evaluate NSC differentiation efficiency on the different substrates, lineage-specific marker immunostainings were performed. After only 3 days of differentiation, cells on Matrigel exhibited significantly higher expression of neuron marker Tuj1 compared to PLL (PLL vs Matrigel: 14.52 ± 3.67% vs 56.05 ± 4.34%, $n = 3$, $P = 0.0007$) (Figure S4A). This trend persisted after 7 days of differentiation, where Tuj1-positive cells remained stable on

Matrigel (52.82 ± 6.97%) but increased on PLL (31.09 ± 2.66%, $n = 3$, $P = 0.0435$) (Figure 3A), implying that Matrigel promotes more efficient and earlier NSC differentiation into neurons than PLL. Conversely, astrocyte marker GFAP-positive cells were significantly fewer on Matrigel (26.97 ± 3.44%) compared to PLL (57.22 ± 2.07%, $n = 3$, $P = 0.0017$) after 7 days of differentiation, indicating PLL is more suitable for NSC differentiation into astrocytes. The expression of oligodendrocyte markers, Olig2 and MBP, showed no significant difference between the groups (Olig2, $P = 0.8701$; MBP, $P = 0.9209$, $n = 3$) (Figure S4B). These results highlight the differential regulation of substrates on NSC differentiation, with Matrigel promoting neural differentiation while PLL favoring astroglial differentiation.

Next, we investigated the substrate influence on the development of NSC-derived neurons by examining neurite outgrowth. Neurite tracing analysis showed that NSC-derived neurons on Matrigel exhibited approximately 1.62 times longer total neurite length (407.39 ± 27.31 μm) compared to PLL (250.05 ± 37.26 μm, $P = 0.0018$) (Figure 3B and Figure S4C). In addition, neurons on Matrigel showed longer longest neurites and more primary branches, branch points, and branch tips. The DCI was 2.12 times higher on Matrigel (785.72 ± 102.57) than on PLL (370.84 ± 52.85, $P = 0.0012$). Sholl analysis also showed more intersections at various distances from the soma on Matriegl compared to PLL ($P < 0.0001$) (Figure 3C). These results indicate a more complex branching pattern of NSC-derived neurons on Matrigel.

Given that mature neurite outgrowth provides the basis for synaptic connection formation during long-term differentiation, we conducted immunostaining for synaptophysin, a presynaptic protein, after 7 and 14 days of differentiation (Figure 3D and Figure S5A). By day 14, neurons on Matrigel exhibited a higher count of synaptophysin puncta compared to PLL (PLL vs Matrigel (per 50 μm): 13.38 ± 0.74 vs 19.13 ± 1.29, $P = 0.0001$), indicating more synaptic connections on Matrigel. Overall, while neurons formed synaptic connections on both substrates, Matrigel notably promoted more mature synapse development of NSCs-derived neurons.

3.4. Physiological Maturation of NSC-Derived Neurons on PLL and Matrigel. Establishing synaptic connections among neurons facilitates the transmission of electrical signals, enabling elaborate neural network development.[37] We then conducted whole-cell patch clamp recordings after 14 days of differentiation to record spontaneous postsynaptic activity, reflecting the functional connectivity of the neuronal network (Figure 4A). Postsynaptic currents (PSCs) were observed in all recorded neurons. Interestingly, we identified two distinct types of currents in both groups. One exhibited PSC as a single peak (indicated by arrows in Figure 4A), referred to as monophasic PSC. The other type comprised multiple overlapping currents, leading to longer duration and larger amplitude compared to monophasic PSC, referred to as multiphasic PSC (indicated by arrowheads in Figure 4A and magnified in Figure S5B).[38] The Matrigel group displayed a significantly higher frequency of monophasic PSCs (1.66 ± 0.39 Hz) compared to PLL (0.08 ± 0.02 Hz, $P = 0.0151$) (Figure 4B). Moreover, the integral area of multiphasic PSCs in the Matrigel group was approximately 3 times larger than that observed in the PLL group, suggesting the possibility of simultaneous release of more neurotransmitters. However, no significant differences were observed in the amplitudes of both monophasic ($P = 0.2007$) and multiphasic PSCs ($P = 0.1471$) between the two groups (Figure S5C). Typically, PSC frequency relates to presynaptic release probability, while amplitude depends on postsynaptic receptor sensitivity. Hence, the increased PSC events in neurons on Matrigel may be attributed to the more synaptic connection, as shown above (Figure 3D).

Another crucial physiological function for neuronal communication and information processing is the generation and transmission of electrical signals, also known as APs. *In vivo* neurons exhibit electrophysiological property shifts with maturation, marked by increased capacitance, hyperpolarization of the resting membrane potential (RMP), and decreased input resistance.[39] We observed these developmental changes *in vitro* for both groups (Figure 4C). Notably, after 14 days of differentiation, neurons on Matrigel exhibited a 1.93-fold higher capacitance compared to those on PLL (Matrigel vs PLL: 29.79 ± 2.24 pF vs 15.45 ± 1.29 pF, $P < 0.0001$). In addition, the RMP of neurons on Matrigel was more hyperpolarized than those on PLL at both day 7 (Matrigel vs PLL: −43.14 ± 4.50 mV vs −27.33 ± 0.82 mV, $P = 0.0004$) and day 14 (Matrigel vs PLL: −54.45 ± 1.29 mV vs −42.08 ± 2.18 mV, $P = 0.0008$). Furthermore, the input resistance of neurons on Matrigel (955.4 ± 167.8 MΩ) was significantly lower than that of neurons on PLL (1879 ± 207.4 MΩ, $P = 0.0214$) after 14 days of differentiation. These findings suggest that neurons on Matrigel exhibit more mature passive membrane properties compared to those on PLL.

We further explore neuron excitability by injecting step-depolarizing currents to induce APs (Figure 4D). After 7 days of differentiation, all recorded neurons on Matrigel (7 out of 7) and 3 out of 7 neurons on PLL could generate repetitive firing of APs in response to depolarizing current steps. By day 14, all recorded neurons in both groups exhibited repetitive AP firing. Specifically, 80% of neurons on Matrigel exhibited tonic firing without noticeable accommodation to the injected current (Figure 4E). In contrast, only 10% of neurons on PLL displayed tonic firing, with others showing adapting firing patterns as the injected current intensity increased. Moreover, neurons on Matrigel fired more APs compared to those on PLL after 14 days of differentiation (Figure S5D). The AP threshold became more hyperpolarized and the amplitude increased with differentiation in neurons on both substrates (Figure S5E), but no significant difference between the two groups was observed. Previous studies have reported that transition from adaptive to tonic firing and increased firing rate are maturation dependent.[39,40] Therefore, these results indicate that NSC-derived neurons on Matrigel develop more mature electrophysiological functions compared to those on PLL.

3.5. Gene Transcriptional Divergence of NSCs on PLL and Matrigel. To investigate how different substrates regulate NSC behavior at the molecular level, RNA-seq transcriptome analysis was performed to detect the gene expression in NSCs on Matrigel and PLL after 7 days of differentiation. Principal component analysis (PCA) exhibited consistent clustering of three biological replicates within each group, revealing stark differences in gene expression patterns between PLL and Matrigel groups (Figure S6A). Compared to the PLL group, 1264 upregulated and 82 downregulated DEGs were identified in the Matrigel group (Figure S6B). GO enrichment analysis uncovered that upregulated genes in the PLL group were related to metabolic processes such as "amino acid metabolic process", "glutathione metabolic process", and "hormone metabolic process" (Figure 5A). Specifically, "glial cell

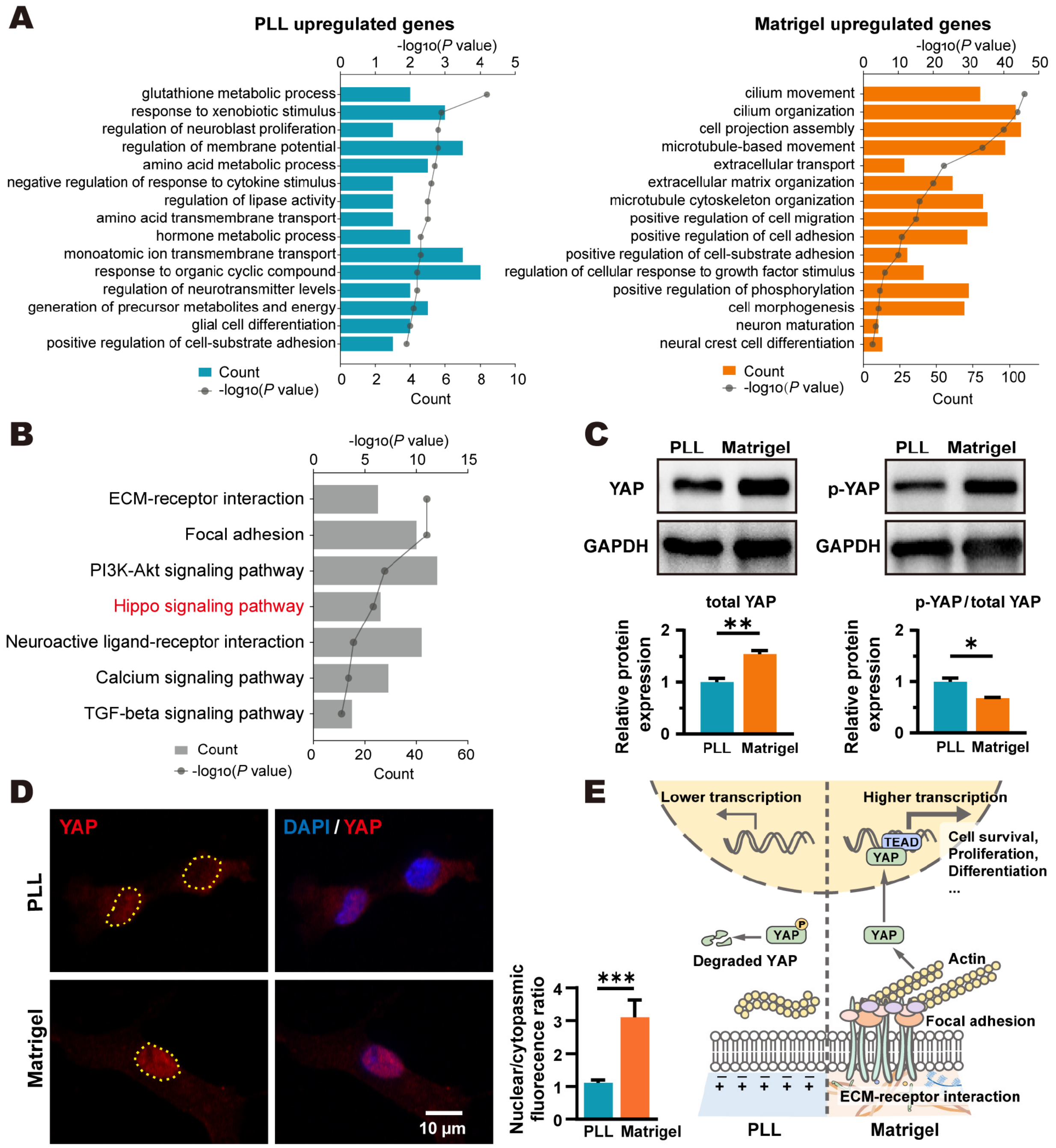

Figure 5. The effect of different substrates on gene expression of NSC. (A) GO biological process enrichment analysis of upregulated DEGs in the PLL and Matrigel groups, respectively. (B) KEGG pathway enrichment analysis of all DEGs. (C) Western blot detection of total and phosphorylated (p)-YAP. $n = 3$. (D) Fluorescence images of YAP (red) and nucleus (stained with DAPI) and quantification of nuclear/cytoplasmic fluorescence ratio. The yellow dotted line indicates the nucleus. PLL, $n = 58$ cells; Matrigel, $n = 63$ cells. (E) Schematic diagram illustrating molecular regulation of NSCs by PLL and Matrigel substrates. Two-tailed unpaired Student's t test. All data are presented as mean ± s.e.m. $^{*}P < 0.05$, $^{**}P < 0.01$, $^{***}P < 0.001$.

differentiation" was enriched, involving genes *Agt*, *Cspg5*, *Hapln3*, and *Fa2h*. These genes are associated with nervous system development and potentially explain PLL's promotion of NSC differentiation into astrocytes. On the other hand, the Matrigel group exhibited a completely distinct transcriptional profile. Biological processes related to cell adhesion were remarkably enriched, including "regulation of cell−substrate adhesion", "positive regulation of cell−substrate adhesion", "cell-matrix adhesion", "focal adhesion assembly" and "cell adhesion mediated by integrin". Moreover, there was a noticeable upregulation of genes governing various NSC growth behaviors, including "regulation of substrate adhesion-dependent cell spreading", "positive regulation of cell migration", "positive regulation of cell population proliferation", "neuron differentiation" and "neuron maturation" (Figure S7). These findings support previous experimental results demonstrating Matrigel's significant enhancement of NSC adhesion, spreading, migration, proliferation and neuronal differentiation.

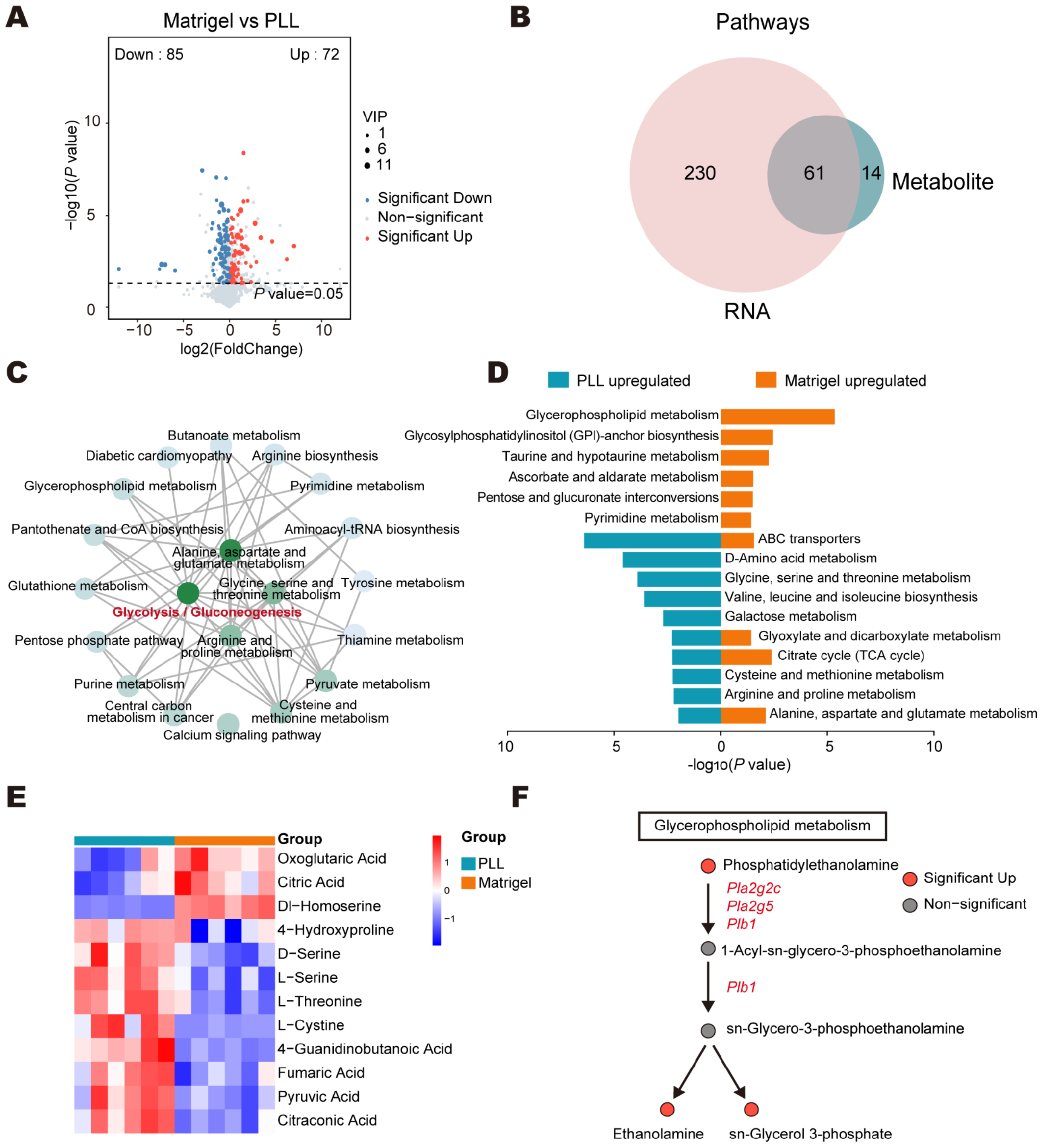

Figure 6. Metabolic profiles of NSC differentiation on PLL and Matrigel. (A) Volcano plot showing upregulated (red) and downregulated (blue) DEMs in Matrigel group compared to PLL. DEMs were identified with VIP values >1.0 and *P* values <0.05. (B) Venn gram of DEG and DEM-mapped KEGG pathways. (C) KGML network of the top 20 interaction pathways, with darker node colors indicating a higher number of interactions. (D) KEGG pathway enrichment analysis of upregulated metabolites in the PLL and Matrigel groups, respectively. (E) Heatmap of DEMs from the enriched amino acid metabolic pathways. (F) DEMs and DEGs in the glycerophospholipid metabolism pathway. Red indicates upregulated and gray indicates not significant.

We then conducted a KEGG pathway enrichment analysis on all DEGs to uncover the signaling pathways modulated by these substrates (Figure 5B). Notably, the ECM-receptor interaction and focal adhesion pathway emerged with the most significant *P* value. Within the "ECM-receptor interaction" pathway, genes encoding the ECM proteins, including laminin, collagen, fibronectin, nephronectin, thrombospondin, tenascin, vitronectin, and the cell surface receptor integrins were upregulated in the Matrigel group (Figure S8). Further GSEA focusing on the Reactome pathway also unveiled that several specific interactions were significantly upregulated in the Matrigel group, including "integrin cell surface interactions", "laminin interactions", "nonintegrin membrane-ECM interactions", and "NCAM1 interactions" (Figure S9). In contrast, we did not observe that such cell—substrate interactions were upregulated in the PLL groups. Consistent with previous studies,[20,41] the results confirm the vital role of integrins in cell adhesion on Matrigel and offer novel insights into the molecular effects of Matrigel on NSCs.

The signals generated by the ECM-receptor interaction require transmission to the nucleus via intracellular signaling pathways to regulate cellular behavior. Hence, we explored downstream signaling pathways. Notably, the Hippo signaling pathway, an important mechanotransduction pathway and also a downstream signaling pathway for focal adhesion,[42] was enriched (Figure 5B), with a wide upregulation of its associated genes (Figure S10). Given the pivotal role of YAP, a key transcriptional regulator in the Hippo signaling pathway, in regulating NSC proliferation and differentiation,[43,44] we assessed YAP activity in NSCs on PLL and Matrigel. Phosphorylated YAP is degraded in the cytoplasm, while unphosphorylated YAP (active status) translocates to the nucleus to interact with TEAD transcription factors to regulate transcription. Thus, we performed Western blot and immunofluorescence analyses to assess YAP levels and subcellular localization. The results revealed a lower relative phosphorylation ratio of YAP (p-YAP/total YAP), higher total YAP levels, and increased nuclear/cytoplasmic fluorescence ratio in the Matrigel group compared to the PLL group (Figure 5C and 5D). This suggests that the YAP protein is more active in the Matrigel group compared to the PLL group. Subsequently, we conducted transcription factor prediction analysis on all DEGs, and the top predicted transcription factor, TEAD, is precisely downstream of YAP.[42] Moreover, approximately one-third of the DEGs (424 genes) were predicted to be regulated by TEAD, encompassing genes associated with cell adhesion, migration, proliferation, and axon extension (Table S1). Recent reports highlight that YAP responds to various biochemical and biophysical signals from the cellular microenvironment, including soluble factors (such as EGF), substrate stiffness, and topology. Additionally, cell changes like cell spreading, focal adhesion formation, and heightened cytoskeletal tension can also activate YAP.[42,45−47] Therefore, we propose that the diverse signals from PLL and Matrigel trigger varying cell shapes, focal adhesion patterns, and cytoskeletal tension. These variations likely result in distinct YAP signaling pathway activity, leading to differences in the transcriptional regulation of a series of genes related to cellular behavior between NSCs on PLL and Matrigel (Figure 5E).

3.6. Metabolic Profiles of NSC Differentiation on PLL and Matrigel. The RNA-seq analysis revealed distinct regulation of multiple genes associated with metabolic processes between PLL and Matrigel (Figure 5A). Given the known important regulation of metabolic activity on NSC fate,[48,49] we conducted metabolomics to elucidate how these substrates regulate NSC metabolism. An integrated untargeted metabolomic analysis using GC-MS and LC-MS was performed after 7 days of differentiation. OPLS-DA showed good clustering within groups and significant variability between the PLL and Matrigel groups (Figure S11A). 7-fold cross-validations and 200 response permutation testing suggested that the OPLS-DA model was valid without overfitting (Figure S11B). We identified a total of 1925 metabolites and 157 DEMs between the two groups. Compared to the PLL group, 72 upregulated and 85 downregulated metabolites were found in the Matrigel group, as illustrated in the volcano plot (Figure 6A) and heatmap (Figure S11C). These results clearly show the distinct metabolic activities of NSCs in response to varying substrates during the differentiation process.

We conducted an integrated analysis of metabolomics and transcriptomics.[50] DEGs and DEMs were mapped onto KEGG pathways, unveiling a total of 61 pathways containing both DEGs and DEMs (Figure 6B). KEGG Markup Language (KGML) network analysis revealed the interaction network among these pathways, with "glycolysis/gluconeogenesis" displaying the most significant interactions with 19 downstream pathways (depicted in Figure 6C). Within the glycolysis/gluconeogenesis pathways, pyruvate acid, a critical connection between glycolysis and oxidative phosphorylation, along with genes regulating glucose homeostasis like *Pklr*, *Hkdc1*, *Eno4*, and *Gck*, exhibits differential expression between PLL and Matrigel groups (Figure S12A). Given that glycolysis stands as a distinctive metabolic trait of NSCs, and its modulation—specifically the shift toward oxidative phosphorylation—serves as one of the most vital NSC differentiation mechanisms,[51] this divergence suggests potential variations in glycolytic metabolism that might contribute to the different effects of substrates on NSC differentiation.

Pathway enrichment analysis on upregulated metabolites in each group further delineates the specific pathways affected by PLL and Matrigel. The top 10 enriched pathways are shown in Figure 6D. Notably, consistent with the enrichment of "amino acid metabolic process" among DEGs upregulated by PLL in the RNA-seq analysis (Figure 5A), several amino acid metabolic pathways were similarly enriched among DEM upregulated by PLL, including "D-amino acid metabolism", "glycine, serine and threonine metabolism", "valine, leucine and isoleucine biosynthesis", "cysteine and methionine metabolism", "arginine and proline metabolism", "alanine, aspartate and glutamate metabolism", and "phenylalanine metabolism". The specific differential amino acids within these pathways are depicted in Figure 6E. It is worth noting that D-serine and its precursor L-serine were upregulated in the PLL group. Considering that L-serine is primarily synthesized by astrocytes, this result may mutually corroborate our observation that PLL promotes NSC differentiation into astrocytes (Figure 3A). Previous studies have highlighted that arginine and branched-chain amino acids (such as valine, leucine, and isoleucine) play a role in regulating the metabolic shift from glycolysis to oxidative phosphorylation during NSC differentiation.[49,52] The modulation of various amino acid metabolism by PLL, as evidenced by both transcriptional and metabolic alterations, could potentially exert further influence on NSC differentiation.

Glycerophospholipid metabolism is the most significantly enriched pathway among the DEMs upregulated by Matrigel. This pathway includes the upregulated DEMs such as phosphatidylethanolamine (PE), ethanolamine, and sn-glycerol 3-phosphate (Figure S12B). Correspondingly, the genes *Pla2g2c*, *Pla2g5*, and *Plb1*, encoding phospholipase enzymes, were also upregulated. These enzymes are involved in the degradation of PE to ethanolamine and sn-glycerol 3-phosphate (as illustrated in Figure 6F). PE, the second most abundant phospholipid in mammalian cells, increases cell membrane fluidity and plays an essential role in various cellular processes, including synaptogenesis, neurotransmitter release, and more. Thus, we hypothesize that the active PE metabolism might contribute to the more mature neural differentiation process in the Matrigel group. Collectively, these findings present novel evidence emphasizing the distinct regulatory impacts of PLL and Matrigel on NSC metabolism. This divergence, coupled with transcriptional alterations, significantly contributes to the diverse regulatory mechanisms governing cell behavior.

4. CONCLUSION

This study presents a comprehensive analysis of the biochemical and biophysical properties of poly-L-lysine (PLL) and Matrigel, delineating their respective influences on NSC fate. We elucidated the mechanisms underlying these effects, particularly focusing on cellular transcription and metabolic pathways. Our findings reveal that Matrigel, characterized by its lower modulus and higher surface roughness, significantly upregulated glycerophospholipid metabolism and enhanced ECM-receptor interactions which facilitated the activation of the transcriptional regulator YAP, thereby markedly promoting cellular adhesion, spreading, migration, and proliferation. Moreover, Matrigel predominantly directed NSC differentiation toward functional neurons. In contrast, PLL was found to upregulate genes associated with glial cell differentiation and amino acid metabolism, and to elevate various amino acid levels, potentially driving the preferential NSC differentiation into astrocytes.

The exploration of interactions between substrates and NSCs, as a means to regulate cellular function and induce multidirectional differentiation, remains a focal point in neuroscientific research. Our study provides novel cellular and molecular insights into the differential behaviors of NSCs on PLL and Matrigel substrates. These findings offer a refined understanding of these traditional surface coatings, paving the way for their optimized and targeted application in NSC research.

■ ASSOCIATED CONTENT

Supporting Information

The Supporting Information is available free of charge at https://pubs.acs.org/doi/10.1021/acsami.4c02575.

> Supplementary figures, include material characterization, cell viability, migration assay, fluorescence experiment results, electrophysiology assay, RNA-seq, and metabolomic analysis results (PDF)
>
> Results of predicted transcription factor and its target genes (XLSX)

■ AUTHOR INFORMATION

Corresponding Authors

Chunyan Li − *Shanghai Key Laboratory of Sleep Disordered Breathing, Department of Otolaryngology-Head and Neck Surgery, Otolaryngology Institute of Shanghai Jiao Tong University, Shanghai Sixth People's Hospital Affiliated to Shanghai Jiao Tong University School of Medicine, Shanghai 200233, China;* orcid.org/0000-0002-8449-9560; Email: 7250012693@shsmu.edu.cn

Shankai Yin − *Shanghai Key Laboratory of Sleep Disordered Breathing, Department of Otolaryngology-Head and Neck Surgery, Otolaryngology Institute of Shanghai Jiao Tong University, Shanghai Sixth People's Hospital Affiliated to Shanghai Jiao Tong University School of Medicine, Shanghai 200233, China;* orcid.org/0000-0003-3689-8599; Email: yinshankai@china.com

Authors

Cuiping Wu − *Shanghai Key Laboratory of Sleep Disordered Breathing, Department of Otolaryngology-Head and Neck Surgery, Otolaryngology Institute of Shanghai Jiao Tong University, Shanghai Sixth People's Hospital Affiliated to Shanghai Jiao Tong University School of Medicine, Shanghai 200233, China;* orcid.org/0009-0008-8531-5381

Suru Liu − *Shanghai Key Laboratory of Sleep Disordered Breathing, Department of Otolaryngology-Head and Neck Surgery, Otolaryngology Institute of Shanghai Jiao Tong University, Shanghai Sixth People's Hospital Affiliated to Shanghai Jiao Tong University School of Medicine, Shanghai 200233, China*

Lei Zhou − *Department of Otorhinolaryngology-Head and Neck Surgery, Zhongshan Hospital Affiliated to Fudan University, Shanghai 200032, China*

Zhengnong Chen − *Shanghai Key Laboratory of Sleep Disordered Breathing, Department of Otolaryngology-Head and Neck Surgery, Otolaryngology Institute of Shanghai Jiao Tong University, Shanghai Sixth People's Hospital Affiliated to Shanghai Jiao Tong University School of Medicine, Shanghai 200233, China*

Quanjun Yang − *Department of Pharmacy, Shanghai Sixth People's Hospital Affiliated to Shanghai Jiao Tong University School of Medicine, Shanghai 200233, China*

Yaqi Cui − *Shanghai Key Laboratory of Sleep Disordered Breathing, Department of Otolaryngology-Head and Neck Surgery, Otolaryngology Institute of Shanghai Jiao Tong University, Shanghai Sixth People's Hospital Affiliated to Shanghai Jiao Tong University School of Medicine, Shanghai 200233, China*

Ming Chen − *Shanghai Key Laboratory of Sleep Disordered Breathing, Department of Otolaryngology-Head and Neck Surgery, Otolaryngology Institute of Shanghai Jiao Tong University, Shanghai Sixth People's Hospital Affiliated to Shanghai Jiao Tong University School of Medicine, Shanghai 200233, China*

Linpeng Li − *Shanghai Key Laboratory of Sleep Disordered Breathing, Department of Otolaryngology-Head and Neck Surgery, Otolaryngology Institute of Shanghai Jiao Tong University, Shanghai Sixth People's Hospital Affiliated to Shanghai Jiao Tong University School of Medicine, Shanghai 200233, China*

Bingbing Ke − *Shanghai Key Laboratory of Sleep Disordered Breathing, Department of Otolaryngology-Head and Neck Surgery, Otolaryngology Institute of Shanghai Jiao Tong University, Shanghai Sixth People's Hospital Affiliated to Shanghai Jiao Tong University School of Medicine, Shanghai 200233, China*

Complete contact information is available at: https://pubs.acs.org/10.1021/acsami.4c02575

Author Contributions

[‖]C.W., S.L., and L.Z. contributed equally to this work. C.W. performed the majority of experiments and wrote the original draft. S.L. and L.Z. performed the experiments and data processing. Y.C., M.C., and B.K. assisted with the experiments. Z.C., L.L. and Q.Y. revised the manuscript. C.L. and S.Y. conceived of the study, designed the study, and reviewed the manuscript. All authors have given approval to the final version of the manuscript.

Funding

This work was supported by the Excellent Young Scientists Fund of the Natural Science Foundation of China (82322020), the National Natural Science Foundation of China (82071042, 82000980), and the Shanghai Pujiang Program (22PJD050).

Notes

The authors declare no competing financial interest.

REFERENCES

(1) Liu, D. D.; He, J. Q.; Sinha, R.; Eastman, A. E.; Toland, A. M.; Morri, M.; Neff, N. F.; Vogel, H.; Uchida, N.; Weissman, I. L. Purification and Characterization of Human Neural Stem and Progenitor Cells. *Cell* **2023**, *186* (6), 1179−1194.e15.

(2) Hayashi, Y.; Lin, H.-T.; Lee, C.-C.; Tsai, K.-J. Effects of Neural Stem Cell Transplantation in Alzheimer's Disease Models. *Journal of Biomedical Science* **2020**, *27* (1), 29.

(3) Zhang, B.; Yan, W.; Zhu, Y.; Yang, W.; Le, W.; Chen, B.; Zhu, R.; Cheng, L. Nanomaterials in Neural-Stem-Cell-Mediated Regenerative Medicine: Imaging and Treatment of Neurological Diseases. *Adv. Mater.* **2018**, *30* (17), No. e1705694.

(4) Hu, Y.; Chen, Z.; Wang, H.; Guo, J.; Cai, J.; Chen, X.; Wei, H.; Qi, J.; Wang, Q.; Liu, H.; Zhao, Y.; Chai, R. Conductive Nerve Guidance Conduits Based on Morpho Butterfly Wings for Peripheral Nerve Repair. *ACS Nano* **2022**, *16* (2), 1868−1879.

(5) Marques-Almeida, T.; Lanceros-Mendez, S.; Ribeiro, C. State of the Art and Current Challenges on Electroactive Biomaterials and Strategies for Neural Tissue Regeneration. *Adv. Healthcare Mater.* **2024**, *13* (1), No. e2301494.

(6) Zhang, H.; Guo, J.; Wang, Y.; Shang, L.; Chai, R.; Zhao, Y. Natural Polymer-Derived Bioscaffolds for Peripheral Nerve Regeneration. *Adv. Funct. Mater.* **2022**, *32* (41), No. 2203829.

(7) Zhang, H.; Wang, H.; Wen, B.; Lu, L.; Zhao, Y.; Chai, R. Ultrasound-Responsive Composited Conductive Silk Conduits for Peripheral Nerve Regeneration. *Small Structures* **2023**, *4* (9), No. 2300045.

(8) Zhang, H.; Qin, C.; Shi, Z.; Xue, J.; Hao, J.; Huang, J.; Du, L.; Lu, H.; Wu, C. Bioprinting of Inorganic-Biomaterial/Neural-Stem-Cell Constructs for Multiple Tissue Regeneration and Functional Recovery. *National Science Review* **2024**, *11* (4), No. nwae035.

(9) Frederico, B.; Martins, I.; Chapela, D.; Gasparrini, F.; Chakravarty, P.; Ackels, T.; Piot, C.; Almeida, B.; Carvalho, J.; Ciccarelli, A.; Peddie, C. J.; Rogers, N.; Briscoe, J.; Guillemot, F.; Schaefer, A. T.; Saúde, L.; Reis e Sousa, C. Dngr-1-Tracing Marks an Ependymal Cell Subset with Damage-Responsive Neural Stem Cell Potential. *Developmental Cell* **2022**, *57* (16), 1957.

(10) Hao, M.; Zhang, Z.; Liu, C.; Tian, Y.; Duan, J.; He, J.; Sun, Z.; Xia, H.; Zhang, S.; Wang, S.; Sang, Y.; Xing, G.; Liu, H. Hydroxyapatite Nanorods Function as Safe and Effective Growth Factors Regulating Neural Differentiation and Neuron Development. *Adv. Mater.* **2021**, *33* (33), No. e2100895.

(11) Hu, H.-B.; Song, Z.-Q.; Song, G.-P.; Li, S.; Tu, H.-Q.; Wu, M.; Zhang, Y.-C.; Yuan, J.-F.; Li, T.-T.; Li, P.-Y.; Xu, Y.-L.; Shen, X.-L.; Han, Q.-Y.; Li, A.-L.; Zhou, T.; Chun, J.; Zhang, X.-M.; Li, H.-Y. Lpa Signaling Acts as a Cell-Extrinsic Mechanism to Initiate Cilia Disassembly and Promote Neurogenesis. *Nat. Commun.* **2021**, *12* (1), 662.

(12) Hu, X.-L.; Chen, G.; Zhang, S.; Zheng, J.; Wu, J.; Bai, Q.-R.; Wang, Y.; Li, J.; Wang, H.; Feng, H.; Li, J.; Sun, X.; Xia, Q.; Yang, F.; Hang, J.; Qi, C.; Phoenix, T. N.; Temple, S.; Shen, Q. Persistent Expression of Vcam1 in Radial Glial Cells Is Required for the Embryonic Origin of Postnatal Neural Stem Cells. *Neuron* **2017**, *95* (2), 309−309.

(13) Giordano, A. M. S.; Luciani, M.; Gatto, F.; Abou Alezz, M.; Beghè, C.; Della Volpe, L.; Migliara, A.; Valsoni, S.; Genua, M.; Dzieciatkowska, M.; Frati, G.; Tahraoui-Bories, J.; Giliani, S. C.; Orcesi, S.; Fazzi, E.; Ostuni, R.; D'Alessandro, A.; Di Micco, R.; Merelli, I.; Lombardo, A.; Reijns, M. A. M.; Gromak, N.; Gritti, A.; Kajaste-Rudnitski, A. DNA Damage Contributes to Neurotoxic Inflammation in Aicardi-Goutières Syndrome Astrocytes. *Journal of Experimental Medicine* **2022**, *219* (4), No. e20211121.

(14) Dang, J.; Tiwari, S. K.; Agrawal, K.; Hui, H.; Qin, Y.; Rana, T. M. Glial Cell Diversity and Methamphetamine-Induced Neuroinflammation in Human Cerebral Organoids. *Molecular Psychiatry* **2021**, *26* (4), 1194−1207.

(15) Bailus, B. J.; Scheeler, S. M.; Simons, J.; Sanchez, M. A.; Tshilenge, K.-T.; Creus-Muncunill, J.; Naphade, S.; Lopez-Ramirez, A.; Zhang, N.; Lakshika Madushani, K.; Moroz, S.; Loureiro, A.; Schreiber, K. H.; Hausch, F.; Kennedy, B. K.; Ehrlich, M. E.; Ellerby, L. M. Modulating Fkbp5/Fkbp51 and Autophagy Lowers Htt (Huntingtin) Levels. *Autophagy* **2021**, *17* (12), 4119−4140.

(16) Gong, L.; Cao, L.; Shen, Z.; Shao, L.; Gao, S.; Zhang, C.; Lu, J.; Li, W. Materials for Neural Differentiation, Trans-Differentiation, and Modeling of Neurological Disease. *Adv. Mater.* **2018**, *30* (17), No. e1705684.

(17) Liao, M.; Hu, Y.; Zhang, Y.; Wang, K.; Fang, Q.; Qi, Y.; Shen, Y.; Cheng, H.; Fu, X.; Tang, M.; Sun, S.; Gao, X.; Chai, R. 3d Ti3c2tx Mxene−Matrigel with Electroacoustic Stimulation to Promote the Growth of Spiral Ganglion Neurons. *ACS Nano* **2022**, *16* (10), 16744−16756.

(18) Wang, K.-H.; Liu, C.-H.; Tan, D.-H.; Nieh, M.-P.; Su, W.-F. Block Sequence Effects on the Self-Assembly Behaviors of Polypeptide-Based Penta-Block Copolymer Hydrogels. *ACS Appl. Mater. Interfaces* **2024**, *16* (5), 6674−6686.

(19) Roth, J. G.; Huang, M. S.; Li, T. L.; Feig, V. R.; Jiang, Y.; Cui, B.; Greely, H. T.; Bao, Z.; Paşca, S. P.; Heilshorn, S. C. Advancing Models of Neural Development with Biomaterials. *Nat. Rev. Neurosci.* **2021**, *22* (10), 593−615.

(20) Aisenbrey, E. A.; Murphy, W. L. Synthetic Alternatives to Matrigel. *Nature Reviews Materials* **2020**, *5* (7), 539−551.

(21) Vieira, M. S.; Santos, A. K.; Vasconcellos, R.; Goulart, V. A. M.; Parreira, R. C.; Kihara, A. H.; Ulrich, H.; Resende, R. R. Neural Stem Cell Differentiation into Mature Neurons: Mechanisms of Regulation and Biotechnological Applications. *Biotechnology Advances* **2018**, *36* (7), 1946−1970.

(22) Zheng, M.; Pan, M.; Zhang, W.; Lin, H.; Wu, S.; Lu, C.; Tang, S.; Liu, D.; Cai, J. Poly(A-L-Lysine)-Based Nanomaterials for Versatile Biomedical Applications: Current Advances and Perspectives. *Bioactive Materials* **2021**, *6* (7), 1878−1909.

(23) Stukel, J. M.; Willits, R. K. Mechanotransduction of Neural Cells through Cell−Substrate Interactions. *Tissue Engineering Part B: Reviews* **2016**, *22* (3), 173−182.

(24) Baumann, H. J.; Betonio, P.; Abeywickrama, C. S.; Shriver, L. P.; Leipzig, N. D. Metabolomic and Signaling Programs Induced by Immobilized Versus Soluble Ifn Γ in Neural Stem Cells. *Bioconjugate Chem.* **2020**, *31* (9), 2125−2135.

(25) Bispo, D. S. C.; Jesus, C. S. H.; Marques, I. M. C.; Romek, K. M.; Oliveira, M. B.; Mano, J. F.; Gil, A. M. Metabolomic Applications in Stem Cell Research: A Review. *Stem Cell Reviews and Reports* **2021**, *17* (6), 2003−2024.

(26) Ramosaj, M.; Madsen, S.; Maillard, V.; Scandella, V.; Sudria-Lopez, D.; Yuizumi, N.; Telley, L.; Knobloch, M. Lipid Droplet Availability Affects Neural Stem/Progenitor Cell Metabolism and Proliferation. *Nat. Commun.* **2021**, *12* (1), 7362.

(27) Romani, P.; Valcarcel-Jimenez, L.; Frezza, C.; Dupont, S. Crosstalk between Mechanotransduction and Metabolism. *Nat. Rev. Mol. Cell Biol.* **2021**, *22* (1), 22−38.

(28) Zhu, Y. D.; Ma, X. Y.; Li, L. P.; Yang, Q. J.; Jin, F.; Chen, Z. N.; Wu, C. P.; Shi, H. B.; Feng, Z. Q.; Yin, S. K.; Li, C. Y. Surface Functional Modification by Ti3c2tx Mxene on Plla Nanofibers for Optimizing Neural Stem Cell Engineering. *Adv. Healthcare Mater.* **2023**, *12* (25), No. e2300731.

(29) Danelon, V.; Goldner, R.; Martinez, E.; Gokhman, I.; Wang, K.; Yaron, A.; Tran, T. S. Modular and Distinct Plexin-A4/Farp2/Rac1 Signaling Controls Dendrite Morphogenesis. *J. Neurosci.* **2020**, *40* (28), 5413−5430.

(30) Martocq, L.; Douglas, T. E. L. Amine-Rich Coatings to Potentially Promote Cell Adhesion, Proliferation and Differentiation, and Reduce Microbial Colonization: Strategies for Generation and Characterization. *Coatings* **2021**, *11* (8), 983.

(31) Kohen, N. T.; Little, L. E.; Healy, K. E. Characterization of Matrigel Interfaces During Defined Human Embryonic Stem Cell Culture. *Biointerphases* **2009**, *4* (4), 69−79.

(32) Banerjee, A.; Arha, M.; Choudhary, S.; Ashton, R. S.; Bhatia, S. R.; Schaffer, D. V.; Kane, R. S. The Influence of Hydrogel Modulus on the Proliferation and Differentiation of Encapsulated Neural Stem Cells. *Biomaterials* **2009**, *30* (27), 4695−4699.

(33) Nascimento, L.; Fernandes, C.; Silva, R. M.; Semitela, Â.; de Sousa, B. M.; Marques, P. A. A. P.; Vieira, S. I.; Silva, R. F.; Barroca, N.; Gonçalves, G. Customizing 3d Structures of Vertically Aligned Carbon Nanotubes to Direct Neural Stem Cell Differentiation. *Adv. Healthcare Mater.* **2023**, *12* (26), No. e2300828.

(34) Arima, Y.; Iwata, H. Effect of Wettability and Surface Functional Groups on Protein Adsorption and Cell Adhesion Using Well-Defined Mixed Self-Assembled Monolayers. *Biomaterials* **2007**, *28* (20), 3074−3082.

(35) Ayala, R.; Zhang, C.; Yang, D.; Hwang, Y.; Aung, A.; Shroff, S. S.; Arce, F. T.; Lal, R.; Arya, G.; Varghese, S. Engineering the Cell−Material Interface for Controlling Stem Cell Adhesion, Migration, and Differentiation. *Biomaterials* **2011**, *32* (15), 3700−3711.

(36) Khalili, A.; Ahmad, M. A Review of Cell Adhesion Studies for Biomedical and Biological Applications. *International Journal of Molecular Sciences* **2015**, *16* (8), 18149−18184.

(37) Sanes, J. R.; Zipursky, S. L. Synaptic Specificity, Recognition Molecules, and Assembly of Neural Circuits. *Cell* **2020**, *181* (3), 536−556.

(38) Pampaloni, N. P.; Lottner, M.; Giugliano, M.; Matruglio, A.; D'Amico, F.; Prato, M.; Garrido, J. A.; Ballerini, L.; Scaini, D. Single-Layer Graphene Modulates Neuronal Communication and Augments Membrane Ion Currents. *Nat. Nanotechnol.* **2018**, *13* (8), 755−764.

(39) Larimer, P.; Hasenstaub, A. R. Functional Maturation of Neocortical Inhibitory Interneurons. *In Synapse Development and Maturation* **2020**, 423−442.

(40) Furlan, F.; Taccola, G.; Grandolfo, M.; Guasti, L.; Arcangeli, A.; Nistri, A.; Ballerini, L. Erg Conductance Expression Modulates the Excitability of Ventral Horn Gabaergic Interneurons That Control Rhythmic Oscillations in the Developing Mouse Spinal Cord. *J. Neurosci.* **2007**, *27* (4), 919−928.

(41) Rowland, T. J.; Miller, L. M.; Blaschke, A. J.; Doss, E. L.; Bonham, A. J.; Hikita, S. T.; Johnson, L. V.; Clegg, D. O. Roles of Integrins in Human Induced Pluripotent Stem Cell Growth on Matrigel and Vitronectin. *Stem Cells and Development* **2010**, *19* (8), 1231−1240.

(42) Panciera, T.; Azzolin, L.; Cordenonsi, M.; Piccolo, S. Mechanobiology of Yap and Taz in Physiology and Disease. *Nat. Rev. Mol. Cell Biol.* **2017**, *18* (12), 758−770.

(43) Luo, J.; Li, P. Context-Dependent Transcriptional Regulations of Yap/Taz in Stem Cell and Differentiation. *Stem Cell Research & Therapy* **2022**, *13* (1), 10.

(44) Choe, M. S.; Bae, C. M.; Kim, S. J.; Oh, S. T.; Kown, Y. J.; Choi, W.-y.; Han, H. J.; Baek, K. M.; Chang, W.; Kim, J. S.; Lim, K. S.; Yun, S. P.; Lee, M. Y. Human Embryonic Stem Cell-Specific Role of Yap in Maintenance of Self-Renewal and Survival. *Cell. Mol. Life Sci.* **2022**, *79* (11), 544.

(45) Aragona, M.; Panciera, T.; Manfrin, A.; Giulitti, S.; Michielin, F.; Elvassore, N.; Dupont, S.; Piccolo, S. A Mechanical Checkpoint Controls Multicellular Growth through Yap/Taz Regulation by Actin-Processing Factors. *Cell* **2013**, *154* (5), 1047−1059.

(46) Dupont, S.; Morsut, L.; Aragona, M.; Enzo, E.; Giulitti, S.; Cordenonsi, M.; Zanconato, F.; Le Digabel, J.; Forcato, M.; Bicciato, S.; Elvassore, N.; Piccolo, S. Role of Yap/Taz in Mechanotransduction. *Nature* **2011**, *474* (7350), 179−183.

(47) Totaro, A.; Panciera, T.; Piccolo, S. Yap/Taz Upstream Signals and Downstream Responses. *Nat. Cell Biol.* **2018**, *20* (8), 888−899.

(48) Petrelli, F.; Scandella, V.; Montessuit, S.; Zamboni, N.; Martinou, J.-C.; Knobloch, M. Mitochondrial Pyruvate Metabolism Regulates the Activation of Quiescent Adult Neural Stem Cells. *Science Advances* **2023**, *9* (9), No. eadd5220.

(49) Xu, M.; Guo, Y.; Wang, M.; Luo, X.; Shen, X.; Li, Z.; Wang, L.; Guo, W. L-Arginine Homeostasis Governs Adult Neural Stem Cell Activation by Modulating Energy Metabolism In vivo. *EMBO Journal* **2023**, *42* (6), No. e112647.

(50) Chen, X.; Li, W.; Chen, J.; Zhang, X.; Zhang, W.; Duan, X.; Lei, B.; Huang, R. Transcriptomics Integrated with Metabolomics Reveals 2-Methoxy-1, 4-Naphthoquinone-Based Carbon Dots Induced Molecular Shifts in Penicillium Italicum. *Journal of Fungi* **2022**, *8* (5), 420.

(51) Coelho, P.; Fão, L.; Mota, S.; Rego, A. C. Mitochondrial Function and Dynamics in Neural Stem Cells and Neurogenesis: Implications for Neurodegenerative Diseases. *Ageing Research Reviews* **2022**, *80*, No. 101667.

(52) Bifari, F.; Dolci, S.; Bottani, E.; Pino, A.; Di Chio, M.; Zorzin, S.; Ragni, M.; Zamfir, R. G.; Brunetti, D.; Bardelli, D.; Delfino, P.; Cattaneo, M. G.; Bordo, R.; Tedesco, L.; Rossi, F.; Bossolasco, P.; Corbo, V.; Fumagalli, G.; Nisoli, E.; Valerio, A.; Decimo, I. Complete Neural Stem Cell (NSC) Neuronal Differentiation Requires a Branched Chain Amino Acids-Induced Persistent Metabolic Shift Towards Energy Metabolism. *Pharmacol. Res.* **2020**, *158*, No. 104863.